Emily A. Kelly [1], V. Kaye Thomas [2], Apoorva Indraghanty [1], and Julie L. Fudge [1, 3]

Perigenual and Subgenual Anterior Cingulate Afferents Converge on Common Pyramidal Cells in Amygdala Subregions

Running title: pgACC-sgACC Afferent Interactions

AFFILIATIONS:
1 Department of Neuroscience
2 Department of Pharmacology and Physiology
3 Department of Psychiatry

CONTACT INFORMATION:
Del Monte Institute of Neuroscience
University of Rochester Medical Center
601 Elmwood Avenue
Rochester, NY 14642
julie_fudge@urmc.rochester.edu
585 275 4535

Abstract

The subgenual (sgACC) and pregenual (pgACC) anterior cingulate are important afferents of the amygdala, with different cytoarchitecture, connectivity, and function. The sgACC is associated with arousal mechanisms linked to salient cues, while the pgACC is engaged in conflict decision-making, including in social contexts. We explored their influence on the nonhuman primate amygdala. After placing same-size, small volume tracer injections into sgACC and pgACC of the same hemisphere, we examined terminal fiber distribution to better understand how these different functional systems communicate with the amygdala. The sgACC has broad-based termination patterns in the amygdala; the pgACC has a more restricted pattern which was always nested in sgACC terminals. Overlap occurred in subregions of the accessory basal and basal nuclei, termed 'hotspots'. In triple-labeling confocal studies, the majority of randomly selected CAMKIIα (+) cells (putative amygdala glutamatergic neurons) in 'hotspots' received dual contacts from the sgACC and pgACC. The ratio of dual contacts occurred over a surprisingly narrow range, suggesting a consistent, tight balance of afferent contacts on postsynaptic neurons. We also found that large boutons, which are associated with greater synaptic strength, were approximately 3 times more frequent on sgACC versus pgACC axon terminals, consistent with a ‘driver’ function. Together, the results reveal a nested interaction in which pgACC ('conflict/social monitoring’) terminals converge with the broader sgACC ('salience') terminals at both the mesoscopic and cellular level in 'hotspots'. pgACC and sgACC convergence suggests a flexible way whereby shifts in arousing cues can rapidly influence cognitive computations such as social monitoring.

Significance statement

The subgenual cingulate (sgACC), which mediates ‘internal salience’, perigenual cingulate (pgACC), which mediates ‘conflict monitoring’, and the amygdala are dysregulated in human mood and anxiety disorders. Using dual tracer injections in the same monkey, we found that sgACC inputs broadly project in the amygdala; in contrast, pgACC terminal fields were more restricted and nested in zones containing sgACC terminals (‘hotspots’). In ‘hotspots’, most CAMKIIα + (excitatory) amygdala neurons were contacted by terminals from both regions, with a consistent ratio of pgACC: sgACC dual contacts, suggesting a strict balance of afferent inputs. The interdependency of pgACC and sgACC information streams suggests that shifting 'internal arousal' states can directly shape responses in amygdala neurons involved in higher cognitive networks.

Introduction

Emotional processing involves coding sensory data as biologically relevant, or 'salient', in order for the organism to survive. The amygdala codes the emotional relevance of complex sensory inputs through an intricate network of intrinsic and extrinsic connections. In humans and monkeys, the amygdala is especially sensitive to salient stimuli of a 'social' nature (i.e. facial expression, vocal expressions)(1-6), which supports survival in highly socially interdependent groups. The same neural ensembles in monkey amygdala can code reward associated with both nonsocial and social stimuli (7), indicating a common or overlapping circuitry available for coding 'salience' and 'social' cue evaluation.

In both human and nonhuman primates, the amygdala is a heterogenous structure with evolutionary expansion of nuclei that communicate directly with the cortex (8). The basal and accessory basal nuclei of the amygdala are the key sites of higher processing through strong, reciprocal connections with the prefrontal cortex, in particular the anterior cingulate (ACC) (9-12). In the human and monkey, amygdala-ACC networks are implicated in flexibly and appropriately modulating reward learning(13), threat and extinction learning (14, 15) and learning from social cues (7, 16, 17). The ACC-amygdala connection develops gradually over childhood and adolescence (18, 19), is influenced by early life experience, and is vulnerable to dysregulation in a host of human psychiatric illnesses (20-22).

The primate ACC, including that in human, has multiple subdivisions based on cytoarchitectural, connectional, and functional features (23). The 'subgenual' ACC (sgACC), and 'pregenual' ACC (pgACC) are most connected with the amygdala (11, 12). The sgACC (Brodmann areas 25/14c) is involved in monitoring emotional arousal and autonomic states (23, 24). In contrast, the pregenual ACC (Brodmann areas 24/32) is involved in 'conflict' decision-making, particularly in social contexts (25-30).

In a previous broad-based study that evaluated 'top-down' projections from the PFC to amygdala using retrograde tracer injections, we found that cortical inputs to the amygdala co-project with one another in a hierarchical manner, dictated by the relative granularity of the cortical region of origin (12). The least differentiated cortices (including the sgACC) form a 'foundational circuit' throughout the basal and accessory basal nuclei, upon which increasingly complex information from more differentiated cortical regions (e.g. pgACC) is 'layered' in more restricted amygdala subregions.

In the present study, we took an anterograde tracing approach to specifically test the hypothesis that inputs from 'social and conflict monitoring' nodes of the ACC (i.e. the pgACC)

that project to the amygdala would always occur in the context of foundational 'salience' inputs (sgACC) in the amygdala. We placed injections to area 25 (sgACC 'salience/arousal') and area 24 and 32 (pgACC, 'social and conflict monitoring') nodes of the ACC in the same animal and examined their patterns of segregation and overlap in specific amygdala nuclei. Then, in regions where sgACC and pgACC terminals overlapped, we further investigated patterns of convergence or segregation onto pyramidal cell populations.

Results

General topography of sgACC and pgACC inputs to the amygdala

A total of 7 injections sites were analyzed for this study: 2 single injections into the sgACC, 1 single injection into the pgACC, and 2 pairs of combined injections in the sgACC/pgACC. As shown in Fig. 1, the sgACC comprises areas 25c and 14c of the ACC. This agranular cortex is defined by a lack of granular layer IV. Case 37FR was located most rostrally, with Cases 50FR, 46FS, and 53FR at progressively caudal levels. Injections into the pgACC, which is slightly more differentiated (Fig. 1A), were in either area 24b (Case 46FR) or area 32 (Case 53FS) or encompassed both area 24b and 32 (Case 54FS).

Cases with sgACC (n= 4) and pgACC (n=3) injections were first charted individually to determine general patterns of termination in the amygdala (see Supplementary Fig. 1 for a detailed description of amygdala subdivisions). All injections into the sgACC resulted a broad distribution of anterogradely labeled fibers, specifically in the medial nucleus (M), the lateral nucleus (L), the magnocellular subdivision of the accessory basal nucleus (ABmc), the magnocellular and intermediate subdivisions of the basal nucleus (Bmc, Bi), the medial subdivision of the central nucleus (CeM) and the amygdalostriatal areas (Fig. 2A-C, blue). Scattered labeled fibers existed in the parvicellular subdivision of the basal nucleus (Bpc) and accessory basal nucleus (ABpc), and in the intercalated islands that surrounded the basal nucleus, consistent with previous studies (31). In general, tracer injections into the pgACC resulted in fewer labeled terminals than sgACC injections, and the distribution was more restricted (Fig. 2D-F, red). A single large injection in area 32/24b (case 54FS) using three times the normal injection volume (150 nl) had the most labeled fibers in the amygdala of all pgACC injections. Despite this relatively large injection, labeled terminal fibers were still less dense and more confined than sgACC injections (50 nl). Labeled fibers were found in the accessory basal nucleus, magnocellular subdivision (ABmc) and the basal nucleus, intermediate subdivision (Bi),

and in the medial and lateral subdivisions of the central nucleus (CeM, CeLcn,respectively), and amygdalostriatal area, with few labeled fibers found in other regions.

pgACC and sgACC labeled fibers overlap in amygdala 'hotspots'

Next, paired injections, matched for tracer volumes, were mapped using adjacent sections containing labeled fibers from each ACC node (Case 46 and Case 53, Fig. 3). Tracers injected into the pgACC and sgACC had been 'reversed' for each case to control for possible effects of tracer transport (fluorescein injection into sgACC /fluororuby injections into pgACC for case 46; the reverse was done for case 53). Resulting maps revealed patterns of segregation and convergence of labeled terminals from each site in the same animal. sgACC terminal distribution patterns (blue) were broad, terminating over the rostrocaudal extent of the basal and accessory basal nuclei (and in other nuclei as described above). The pgACC inputs (red) mainly terminated in the specific basal nucleus subregions (Bi > Bmc) and the magnocellular accessory basal nucleus (ABmc). In these regions, they reliably overlapped labeled fibers from the sgACC site. We termed these regions of apparent overlap 'hotspots'. Some overlap was also noted in the medial subdivision of the central nucleus.

Most CAMKIIα (+) cells in 'hotspots' receive dual contacts

For paired injections, we then conducted triple-labeling for each tracer and CAMKIIα (a marker of pyramidal neurons in the amygdala (32)). We used confocal methods to determine the degree of fiber 'contact' onto putative excitatory neurons in both ABmc and Bi 'hotspots' where labeled terminals from both the sgACC and pgACC converged (Fig. 4A-B). Thresholding of randomly selected CAMKIIα(+) cells and tracer labeled fibers was completed in separate channels, and overlaid. The thresholding of CAMKIIα(+) cells was done to maximize resolution of soma/proximal dendrites. We then applied stringent criteria for pre- and post-synaptic structure proximity to define terminal 'contacts' onto post-synaptic CAMKIIα(+) cells (Methods, Fig. 4C-D; Supplemental Fig. 2).

The paired injection cases (cases 46 and 53) each had an injection into sgACC (area 25); case 46 had a companion injection in pgACC (area 24b), and case 53 had a companion injection in pgACC area 32 (Fig. 1). Randomly selected CAMK-IIα(+) cells in each 'hotspot' in each case were examined for contacts with either sgACC or pgACC tracer (+) boutons (Fig. 4A-D). Given some variability in labeled fiber distribution across the rostrocaudal extent of the ABmc and Bi for all tracers/injections at the macroscopic level, we first examined whether there

were differences in numbers of pgACC and sgACC contacts across the entire rostrocaudal expanse in each animal. No rostrocaudal differences were found, and results of all sections were grouped for each animal (data not shown). For all CAMK-IIα(+) cells examined (n=300), there were no significant differences in the number of pgACC and sgACC contacts (sgACC: 247 contacts in ABmc, 244 contacts in Bi; pgACC: 346 contacts in ABmc, 271 contacts in Bi; ANOVA with Tukey's Multiple Comparisons test; $F(3,4)=0.9985$, $p=0.4795$; n.s.). The ratio of pgACC to sgACC labeled contacts was approximately equal in both the ABmc and Bi 'hotspots (Fig.4E, n= 150 total cells ABmc, n=150 total cells Bi, two-tailed students t-test; $p=0.2525$; n.s.).

We then explored the extent to which pgACC and sgACC contacts converged on the same CAMK-IIα(+) cells in each area. The majority of randomly selected CAMK-IIα(+) neurons had contacts from both the sgACC and pgACC, in both ABmc and Bi regions (Fig. 4F, Two-way ANOVA with Tukey multiple comparisons test; DUAL vs all other contact profiles=***= $p<0.001$). There were no significant differences in the distribution of dual-contact CAMK-IIα(+) neurons in the rostrocaudal plane (data not shown). Relatively lower proportions of CAMK-IIα(+) neurons had no contacts from either projection or had contacts from a single projection. These data indicate that the majority of CAMK-IIα(+) neurons in ABmc and Bi 'hotspots' are dually regulated by the sgACC and pgACC afferent contacts.

<u>The proportion of pgACC to sgACC dual contacts are tightly balanced</u>

Since the majority of CAMK-IIα(+) neurons in 'hotspots' had dual contacts, we calculated the relative weighting of sgACC and pgACC contacts on individual dually contacted cells, and the distribution of the ratios of pgACC-to-sgACC contacts throughout the ABmc and Bi populations (Fig. 5 A-B, Supplemental Table 1). Ratios of contacts from each area onto individual CAMK-IIα(+) neurons ranged from 0 to 3.5. The majority of dual pgACC: sgACC contact ratios for both the ABmc and Bi were in a narrow 1.0-1.5 range, suggesting a relatively tight balance of inputs onto individual pyramidal neurons. Given this narrow range, we pooled our data and performed quantification based on ratio bin counts (Fig. 5C). Quantitative comparisons of ratio bin counts display significantly higher counts in the range of 1-1.5 when compared to every other bin (*=$p<0.05$, ****= $p<0.001$, one-way ANOVA with Tukey multiple comparisons post hoc test).

sgACC and pgACC synaptic bouton volumes

We next examined bouton volumes from the sgACC and pgACC in each 'hotspot' as an approximation of synaptic 'strength' (33). Data were collected on terminal boutons and *boutons 'en passant'* using stereologic methods in adjacent, single labeled sections. The majority of boutons were less than 0.52 μm^3 volume (equivalent 1mm. diameter), for both sgACC and pgACC afferents (Fig. 6). However, there was a higher frequency of relatively large terminals for the sgACC in both the ABmc and Bi (Supplementary Table 2 and 3). Using >0.52 μm^3 (> 1mm diameter) as a cut-off for 'large' boutons, we found that the sgACC terminals overall had significantly more large boutons (27-31%) compared to the pgACC (9-10%) (*sgACC*: J46 (total large boutons/total) = 196/617; M53 (total large boutons/total) = 142/509; *pgACC*: J46 (total large boutons/total) = 29/307; M53 (total large boutons/total) = 61/595; p=0.0103; unpaired student t-test). 'Large' bouton comparisons from the same afferent source did not differ significantly across the ABmc and Bi (p=0.9114, unpaired student t-test), suggesting a consistent feature of the projection.

Discussion

We previously showed that prefrontal-amygdala paths are organized in hierarchical arrays, dictated by the degree of laminar differentiation of the cortex (12). To examine this relationship in a more focused way and at the cellular level, we placed anterograde tracer injections into two different nodes of the ACC that have progressive laminar features (pgACC>sgACC), and distinct connections and functions (10 , 34-36). Here, we show at the 'meso-scale' that pgACC afferent terminals are always 'nested' in broader sgACC terminals in the basal and accessory basal nuclei, confirming previous retrograde results, and elucidating connectional principles of the two ACC-amygdala microcircuits.

At the cellular level, we found that the majority CAMIIα (+) amygdala neurons (putative projection neurons) in 'hotspots' were co-contacted by terminals from the sgACC and pgACC. This was true regardless of whether the 'hotspot' was in the ABmc or Bi. Despite the size of the 'hotspots' in the large primate samples, there were no rostrocaudal differences for these findings. Another key finding is that the ratio of pgACC-to-sgACC contacts was highly consistent within and across 'hotspots' and fell mainly in the range of 1.0-1.5. This suggests a general consistency in the relationship in pgACC:sgACC afferent balance onto common post-synaptic cells, at least in normal young Macaques. Finally, sgACC terminals were more likely to

have large boutons, compared to pgACC terminals, suggesting possible differences in transmission speed and efficiency.

Layering of amygdala subcircuits

The agranular sgACC is strongly interconnected with the midline thalamus, hypothalamus and periacqueductal gray, all of which mediate arousing and autonomic components of emotional responses (31, 37). The sgACC has therefore been considered a core node in the 'somatic' marker hypothesis, which states that covert signals from the body (such as autononomic features and visceral sensations) are important in shaping emotions and, eventually, action (38, 39). In contrast, the pgACC (Area 24/32) sits directly and dorsally adjacent to the sgACC and is more organized in its laminar construction. However, the pgACC does not have direct connections to the internal milieu via midline connections like the sgACC, although it shares many of the same 'limbic' connections and receives input from the sgACC (11, 40, 41). The pgACC plays a prominent role in rapid conflict assessment and decision-making, based on studies in monkeys (29, 42, 43) and in the human (30, 44-46). Not surprisingly, the pgACC is activated during tasks involving social decision-making tasks, which are intuitive and rapid and involve predicting outcomes based on social cues such as facial expression (16, 26). The fact that 'salience'-detecting (sgACC) and 'social/conflict- monitoring' (pgACC) components of the ACC have an overlapping, afferent influence in specific 'hotspots' of the ABmc and Bi, suggests that the internal 'salience' information co-regulates amygdala neurons involved in 'conflict monitoring' and decision-making networks.

The amygdala is involved in an array of functions including fear conditioning and extinction (47, 48); safety signaling (49); updating value representations (50); responses to emotion in facial expressions (51-53), and social decision-making and behavior (54-56). Current evidence from chronic recordings in monkeys indicates that the amygdala's capacity to participate in all these tasks and contexts is due to multi-dimensional processing (43, 57). For example, the same amygdala populations that respond to direct eye gaze (a threat cue in nonhuman primates) also respond to non-social aversive stimuli (air-puff) (58). Conversely, neurons that respond to averted eye gaze (a cue predicting submissive, positive social interactions) also respond to juice reward. Amygdala neurons are thus able to flexibly code across social and nonsocial stimuli to predict outcome in specific contexts. The present anatomic findings suggest that this multi-dimensionality may be served by the high rate of

converging contacts on the same amygdala neurons from functionally distinct ACC regions, which may confer flexibility across various stimuli and contexts.

High convergence of sgACC/pgACC contacts on projection neurons

The majority (85%) of cortical afferent inputs terminate onto pyramidal neurons, based on work in rodents (59). Synapses located closest to the soma (or on the soma itself) have the most influence on the overall circuit, as they act to strengthen or weaken the overall cellular response (reviewed in; 60). One of our most striking findings was that sgACC and pgACC terminals target the same pyramidal cell populations, with relatively few pyramidal neurons having only a single contact. Consistent with this finding, functionally related excitatory inputs are often clustered in regards to synaptic placement along the cell and are thought to possibly contribute to coordinated regulation of synaptic plasticity among co-active inputs (61). Through spatial clustering, temporally co-activated excitatory inputs are more likely to initiate a potentiating response within the cell than inputs spaced a distance from one another. Although we did not examine synaptic contacts onto distal dendrites, the finding that dual contacts at the soma/proximal dendrites were the rule, and were tightly balanced in relationship to one another, strongly suggests cooperative actions in regulating post-synaptic cell excitability. The pgACC and sgACC are separate, but closely related brain regions with respect to connectivity and function. They therefore follow this general principle of “coordinated regulation” by functionally related inputs, contributing to the integration of complex or fluid informational streams.

The highly consistent ratio of sgACC to pgACC contacts in normal young animals raises questions about how and when this precise ratio is developed. In mice, the long-range afferents from the medial prefrontal cortex in general arrive in the basal nucleus by postnatal day (PND 10-15) (62, 63), but synaptic strength continues to develop until PND 30 (early adolescence) based on physiologic data. While the development of the relative 'balance' of the sgACC and pgACC (infralimbic and prelimbic cortices in rodents) terminals on the post-synaptic neuron is not known, experience-dependent plasticity likely contributes (64). We speculate that experiences in early life contribute to sgACC:pgACC terminal balance.

A factor in the function of terminals is synapse size. Glutamatergic synapses are classified broadly into Class I and Class II synapses (33). Class I synapses are large (> 1 um diameter), associated with large axons, and release glutamate to affect 'all or none' action potentials. They are considered 'drivers' of the circuit. Larger glutamatergic synapses are associated with larger post-synaptic densities (65), larger axon diameters (66) and greater

transmitter release (67, 68). These structural specializations are thought to prioritize functional inputs in terms of timing and signal strength. In contrast, Class II synapses are smaller and modulatory, and shape post-synaptic excitability. In the present study, a higher number of large boutons in sgACC terminals may confer 'driver' function from sgACC contacts, balanced by pgACC modulators. In future studies, a key question will be to describe sgACC versus pgACC inputs at the ultrastructural level; to determine synaptic size, location (i.e. axo-dendritic spine/shaft, axo-somatic, etc.), and number (i.e single or multiple bouton contacts) (reviewed in, 69)) associated with glutamatergic post-synaptic neurons (70).

Conclusion

The primate amygdala is evolutionarily expanded, accompanied by increased levels of cellular complexity and coding capacity (16, 71, 72). Consistent with its cellular complexity, divergent coding schemes in the primate amygdala operate to facilitate different functions (43). Our results may help explain multi-dimensional coding flexibility of amygdala neurons since broad-based sgACC terminal fields appear capable of driving wide-spread activity in the amygdala. In contrast, pgACC inputs follow a more restricted, nested topography (12) (present results), forming highly convergent contacts on sgACC-recipient neurons in specific ‘hotspots’. This arrangement allows maximum flexibility, with the sgACC providing broad 'internal salience' feedback to the amygdala, but also permitting cooperative signalling with pgACC inputs for conflict monitoring and social decision-making in ‘hotspots’ of convergence.

Materials and Methods

Overall Design

We designated injections that involved Brodmann areas 25 as subgenual anterior cingulate (sgACC) and injections into area 32 and/or 24b as perigenual anterior cingulate (pgACC), respectively. A small injection of a different tracer was placed into the sgACC and pgACC of the same hemisphere in the macaque (Macaque fascicularis). Following sectioning and processing of the brains for tracers using immunocytochemistry, we mapped the distribution of anterogradely labeled afferent fibers within amygdala subregions and used these macroscopic maps to identify regions of terminal segregation and overlap in the amygdala. We then conducted triple immunofluorescent analyses aimed at examining the relationship of axon contacts onto presumptive glutamatergic neurons in regions of terminal overlap. The relative

size of synaptic boutons associated with the sgACC and pgACC in regions of overlap were conducted in single-labeled, adjacent sections using stereologic methods.

Animals and surgery

Injections were stereotaxically placed in 5 male *Macaque fascicularis* (Worldwide Primates, Tallahassee, FL USA) weighing between 3kg and 5.5 kg. Prior to surgery and tracer injection, a T2 anatomical MRI scan using a custom head coil (0.5 x 0.5 x 0.88 millimeter resolution) was acquired on each subject. Thus, each subject had unique coordinates based on individual anatomy. Seven days prior to surgery, animals began a daily course of perioperative gabapentin (25 mg/kg) for preventative pain management. On the day of surgery, the monkey was sedated with intramuscular ketamine (10mg/kg) and then intubated, maintained on 1.5% isoflurane, and stabilized in a surgical stereotaxic apparatus. A craniotomy was performed under sterile conditions. In the majority of cases, small injections (40 nl) of bidirectional tracers tetramethylrhodamine (fluoruby, FR) and fluorescein (FS) were pressure injected over a ten-minute period into the sgACC and/or pgACC of the same hemisphere, using coordinates calculated from the T2 MRI atlas created for that animal. In one animal, a single injection of 150 nl was pressure injected into pgACC for comparison (case MF54FS). For all injections, the syringe was left in place for 20 minutes after each injection to prevent tracking of the tracer up the injection track. Only one tracer injection of each type was made per animal. Following placement of planned injections, the bone flap was replaced, and the surgical site was closed. Post-operative daily monitoring of animals for signs of discomfort was conducted and gabapentin tapered accordingly.

Tissue preparation

Twelve to fourteen days post-surgery, the animals were placed into a deep coma with pentobarbital (initial dose 20 mg/kg via intravenous line). They were sacrificed by intra-cardiac perfusion using 0.9% saline containing 0.5 milliliters of heparin sulfate (200ml/min for 15-20 minutes), followed by cold 4% paraformaldehyde in 0.1M phosphate buffer, pH 7.2 (PB) (200ml/min for 15-20 minutes). Following brain extraction, brains were postfixed overnight in 4% paraformaldehyde solution, then submerged sequentially in 10%, 20%, and 30% sucrose solutions until they sank in each. Brains were sectioned on a freezing, sliding microtome into 40μm sections. Each section was placed sequentially in 24-compartment slide boxes containing

cold cryoprotectant solution (30% sucrose and 30% ethylene glycol in 0.1 M PBS) and stored at -20°C.

Single label immunocytochemistry

To assess the location of anterogradely labeled fibers in amygdala subregions, three adjacent compartments through the amygdala were selected: one for the sgACC tracer, one for the pgACC tracer, and one intervening compartment for acetylcholinesterase (AChE) staining. AChE histochemistry shows clear demarcations of nuclear boundaries in the non-human primate amygdala (73) (Supplemental Fig. 1). Sections were rinsed in 0.1MPB, pH 7.2, with 0.3% Triton-X (PB-TX) overnight. The following day, tissue was treated with endogenous peroxidase inhibitor for five minutes and then thoroughly rinsed with PB-TX, and place in a blocking solution of 10% normal goat serum in PB-TX (NGS-PB-TX) for 30 minutes. Following rinses in PB-TX, tissue was incubated in primary antisera to FR (1:1000, Invitrogen, rabbit) or FS (1:2000, Invitrogen, rabbit) for ~96 hours at 4°C. Tissues were then rinsed with PB-TX, blocked with 10% NGS-PB-TX, incubated in biotinylated secondary anti-rabbit antibody, and then incubated with avidin-biotin complex (Vectastain ABC kit, Vector Laboratories, Burlington, ON Canada). After rinsing, the tracer was visualized with 2,2'-diaminobenzidine (DAB, 0.05mg/ml in 0.1M Tris-buffer). Sections were mounted out of mounting solution (0.5% gelatin in 20% ETOH in double distilled water) onto subbed slides, dried for 3 days, and coverslipped with DPX mounting media (Electron Microscope Sciences, Hatfield, PA).

To determine potential fiber interaction with intercalated neuron populations surrounding the amygdala, additional tracer labeled sections were counterstained with Nissl.

Triple immuno-fluorescent labeling for tracers and CAMK-IIα

To determine the relationship of anterogradely labeled fibers from the peri- and subgenual PFC into the amygdala, we performed triple immunofluorescent staining for each tracer and calmodulin-dependent protein kinase II (CAMK-IIα), a marker of pyramidal cells in the amygdala (32) on an additional series through the amygdala in animals with paired injections. Optimization and specificity of fluorescent staining for all antigens was first conducted in single labeling experiments, with reference to the permanently labeled compartments for tracer (above) and CAMKIIα. Sections were rinsed in 0.1M PB, pH 7.2, with 0.3% Triton-X (PB-TX) overnight. The following day, tissue was treated with endogenous peroxidase inhibitor for 30 minutes and then thoroughly rinsed with PB-TX and placed in a blocking solution of 10% normal

donkey serum in PB-TX (NDS-PB-TX) for 1 hour. Following rinses in PB-TX, tissue was incubated in 3% NDS-PB-TX primary antisera to FR (1:1000, Invitrogen #A6397, *made in rabbit*), FS (1:500, Invitrogen, #A11095, *made in goat*) and CAMK-IIα (1:1,000, Millipore #05-532, *made in mouse*) for ~96 hours at 4°C. Tissues were then rinsed with PB-TX, blocked with 3% NDS-PB-TX and first incubated in biotinylated secondary anti-mouse antibody (1:200, Vector Labs, CAMK-IIα amplification) overnight at 4°C. Tissues were visualized following pooled incubation with donkey anti- rabbit Alexa Fluor 568 (1:200, FR visualization), donkey anti-goat Alexa Fluor 488 (1:100, FS visualization) and Streptavidin 647 (1:200, CAMK-IIα visualization). Tissue was mounted out of 0.1M PB, pH 7.2 and cover-slipped with Prolong Gold anti-fade mounting media (Invitrogen).

Analysis

Charting of anterograde fiber labeling in specific amygdala subregions.

Our injections included both single tracer injections in the sgACC and pgACC in different animals, as well as paired injections in the sgACC/pgACC in the same animal. For all cases, charting of the distribution of anterogradely labeled fibers in specific amygdala subregions was first done on permanently labeled tissue. Anterogradely labeled fibers for each case were visualized using an Olympus BX51 microscope equipped with a darkfield light source. Fibers were manually traced using an attached camera lucida drawing tube using a 4X and 10x objectives. Putative terminal fibers were characterized as thin processes with boutons. Thick labeled fibers without beaded processes were classified as fibers of passage and were not traced. Paper traces were scanned on a flat-bed scanner at high-resolution. Images were imported, stitched together and digitized using Adobe Photoshop CC. AChE-stained adjacent sections were projected onto anterograde traces using a JENA projector and nuclei borders were manually traced with the aid of landmarks within the tissue (i.e. blood vessels) and transferred onto digital files using a drawing tablet interfaced with the Adobe Illustrator CC. Tracer labeled sections and adjacent AChE labeled sections were placed into separate layers of in each file and aligned. Final image digitation and post-processing was performed using Adobe Illustrator CC. For paired injections in the same animal, the relationship of the anterogradely labeled fibers resulting from each injection site, and their localization in specific amygdala subregions, was done by turning off and on the visibility of layers. Regions containing overlap of pgACC and sgACC labeled terminals were identified across the amygdala ('hotspots').

Confocal capture and analysis of interactions between tracer-labeled fibers and CAMK-IIα positive cells.

Cases with paired injections in the sgACC and pgACC and their regions of labeled fiber overlap in the amygdala ('hotspots') were further assessed using high power (confocal) microscopy in conjunction with a semi-automated algorithm to detect and quantify relative numbers of tracer labeled boutons on amygdala CAMK-IIα positive cells. Triple-immunofluorescent images were collected on a Nikon A1R HD Laser Scanning Confocal with NIS-Elements (Center for Advanced Light Microscopy and Nanoscopy) software using tissue landmarks on adjacent AChE-stained sections such as blood vessels for alignment, focusing on regions of interest (ROIs) where tracer labeled fibers overlapped at the light microscopic level. The following excitation lasers (ex) and emission filters (em) were used for confocal imaging: Alexa Fluor 488; ex 488, em 525/50, Alexa Fluor 568; ex 561, em 595/50, Streptavidin 647; ex 640, em 650 LP. Overview images were collected using a 20x/0.75 NA Nikon Plan Apochromat VC objective to locate ROIs in regions of tracer labeled fiber overlap, and z-series stacks were selected and collected using a 60x/ 1.49 NA Nikon Apochromat TIRF objective (xy pixel size of 0.17 micron; z-step size of 0.3 micron). 2-3 ROIs per 'hotspot' were collected per slide in each nucleus (n=2-3 slides; rostral to caudal extent of the amygdala) for each experimental case.

Projection images were analyzed with Imaris 9.6 software (Bitplane). Within each collected image stack (approximately 6-9 stacks per ROI per animal), ten CAMK-IIα positive cells were randomly selected for analysis. XYZ coordinate locations for each analyzed cell were carefully logged. In the 3D module, CAMK-IIα labeling was visualized using the "*surface rendering*" option (grain size=0.345 um diameter). The "smoothing" tool was disabled, as this introduces an artificial uniformity to the cell surface. Next, using the interactive software histogram of Cy5 voxels (volumetric pixels), a threshold was selected to include as much of the neuronal soma and proximal dendrites as possible while excluding any background. A second threshold (interactive size threshold) was next applied to exclude any further extraneous background labeling while still retaining the true volume of the labeled cell. Final renderings were then analyzed in 3D and looked at from all angles. In instances where the labeling was disjointed but clearly part of the actual cell, segments were linked, resulting in an n=10 cells per image.

Fibers were analyzed using the "*spot rendering*" option. In the "slice view", fiber thickness was checked (a line measurement across the entire thickness of the fiber), resulting in

a final size diameter of 2 um for all cases. The sensitivity for selected spots was adjusted using the automatically generated interactive histogram based on voxel size. We selected an area on the histogram to accurately detect as many boutons as possible without creating artifacts. Identical coordinates used during the "*surface rendering*" step were then applied to the "*spot rendering*" steps to ensure a 1:1 registration between the analyzed locations (CAMK-IIα cells) for detection and analysis of tracer labeled boutons. This step was conducted for each tracer labeled bouton, and individually overlaid on the CAMKIIα-positive surface rendering.

Once the combined CAMK-IIα 'surface' rendering and 'spot' renderings for tracer labeled boutons were constructed, we sought to determine the proportion of putative glutamatergic neurons contacted by tracer-labeled spots, including the proportion of CAMK-IIα containing neurons receiving dual-contacts. To do this, we used the "shortest distance" module to filter out all spots that were more than 0.5um from the cell surface. In the Imaris software, spot/surface contacts are based on a measurement from the center of the spot (radius) to the edge of the rendered surface object. As 'spots' were calculated as 2um, a radius of 1um would determine all spots "touching" a surface. Fiber boutons located close to CAMK-IIα cells but not in actual contact, may have an apparent voxel overlap due to the inherent resolution limits of light microscopy (a blurring of fluorescent edge resolution that extends beyond the actual true surface boundary). False-positive contacts can be controlled for by requiring a minimum number of overlapping voxels for an object to be classified as a true contact (74). Our analysis was restricted to a maximum object to surface distance of 0.5um (at least a 50/50 overlap of spot and surface objects; Supplementary Fig. 2) to create a relatively stringent inclusion criteria for assessing 'synaptic contact'. Each CAMK-IIα (+) cell was analyzed in 3D and manual counts were performed in each fluorescent channel. We sought to determine a range of cell-contact types; including (i) no contacts, (ii) individual tracer contacts, and (iii) cells that contained dual contacts (single tracer contacts on the same cell). We present our results as (i) the proportion of pgACC/sgACC contacts on all CAMK-IIα cells and (ii) the percentage of contact type (see description above) onto CAMK-IIα (+) cells across amygdalar nuclei. For CAMK-IIα positive neurons receiving dual contact, we also analyzed the ratio of pgACC to sgACC contacts on each individual cell, presented as the percentage of neurons with different ratios of pgACC:sgACC contacts per 'hotspot' as well as the frequency of those contacts.

Analysis of bouton size from pgACC and sgACC.

To examine the relative size of axonal boutons from the pgACC and sgACC, we used unbiased stereologic methods to survey the basal and accessory basal nucleus 'hotspots' where overlapping terminals were found in each case. Using adjacent sections immunostained for the relevant tracer placed either in the sgACC or pgACC, the general terminal distribution in each 'hotspot' was drawn using a 2x (Plan, NA 0.05 ∞/-) objective. To sample under 100x (UPlanFl, NA 1.3) oil immersion objective, sampling parameters were: grid size 300 x 300, dissector height of 2um and a z-height of 5 um, resulting in sufficient sampling to yield a coefficient of error < 0.10. Axonal varicosities and terminal-like structures are considered synapses, as previous confirmed by electron microscopic methods (75). Both were counted using systematic, random sampling strategies in single-labeled adjacent slides for each tracer. The nucleator method (isotropic), which assumes sphericity of the structure, was applied to measure each putative synaptic structure along the Z axis, in the sampling frame (StereoInvestigator, Microbrightfield Bioscience, Williston, VT). Results were expressed in μm^3. Frequency histograms were created for each tracer in each area, and assessed for shape, spread, and percent of synaptic terminals > 0.52 μm^3 (equivalent to 1 μm diameter).

Statistics

Statistical analyses were performed using Graphpad Prism software (V9.0.2 for Windows, LaJolla, California). A two-tailed unpaired student t-test was used to compare the total number of contacts in each injection group across amygdalar region. Similarly, a two-tailed unpaired student t-test was used to compare pgACC/sgACC ratio means across amygdalar nuclei. A 2x3 two-way ANOVA investigated the relationship of contact type on injection site (pgACC vs sgACC) and ROI (ABmc vs Bi). A two-way ANOVA was used to compare pgACC/sgACC ratio bin means across amygdala nuclei and injection sites. Post-hoc testing was conducted using Tukey's multiple comparison test (Tukey's HSD). $P<0.5$ was deemed statistically significant. Error bars are presented as standard error of the mean.

Data sharing statement

Digital data can be accessed by contacting the corresponding author at: julie_fudge@urmc.rochester.edu.

Funding information

This research was funded by the National Institutes for Mental Health (R01 MH63291).

References

1. K. M. Gothard, F. P. Battaglia, C. A. Erickson, K. M. Spitler, D. G. Amaral, Neural responses to facial expression and face identity in the monkey amygdala. *Journal of neurophysiology* **97**, 1671-1683 (2007).
2. C. P. Mosher, P. E. Zimmerman, K. M. Gothard, Neurons in the monkey amygdala detect eye contact during naturalistic social interactions. *Current biology : CB* **24**, 2459-2464 (2014).
3. S. Wang *et al.*, Neurons in the human amygdala selective for perceived emotion. *Proceedings of the National Academy of Sciences of the United States of America* **111**, E3110-3119 (2014).
4. U. Rutishauser *et al.*, Single-unit responses selective for whole faces in the human amygdala. *Current biology : CB* **21**, 1654-1660 (2011).
5. U. Rutishauser, A. N. Mamelak, R. Adolphs, The primate amygdala in social perception - insights from electrophysiological recordings and stimulation. *Trends in neurosciences* **38**, 295-306 (2015).
6. S. Wang *et al.*, The human amygdala parametrically encodes the intensity of specific facial emotions and their categorical ambiguity. *Nature communications* **8**, 14821 (2017).
7. J. Munuera, M. Rigotti, C. D. Salzman, Shared neural coding for social hierarchy and reward value in primate amygdala. *Nature neuroscience* **21**, 415-423 (2018).
8. H. Stephan, H. D. Frahm, G. Baron, Comparison of brain structure volumes in insectivora and primates VII. Amygdaloid components. *J. Hirnforsch.* **5**, 571-584 (1987).
9. H. T. Ghashghaei, C. C. Hilgetag, H. Barbas, Sequence of information processing for emotions based on the anatomic dialogue between prefrontal cortex and amygdala. *NeuroImage* **34**, 905-923 (2007).
10. S. T. Carmichael, J. L. Price, Limbic connections of the orbital and medial prefrontal cortex in macaque monkeys. *J. Comp. Neurol.* **363**, 615-641 (1995).
11. K. K. Sharma, E. A. Kelly, C. W. Pfeifer, J. L. Fudge, Translating Fear Circuitry: Amygdala Projections to Subgenual and Perigenual Anterior Cingulate in the Macaque. *Cereb Cortex* **30**, 550-562 (2020).
12. Y. T. Cho, M. Ernst, J. L. Fudge, Cortico-Amygdala-Striatal Circuits Are Organized as Hierarchical Subsystems through the Primate Amygdala. *The Journal of neuroscience : the official journal of the Society for Neuroscience* **33**, 14017-14030 (2013).
13. W. Zhang *et al.*, Functional circuits and anatomical distribution of response properties in the primate amygdala. *The Journal of neuroscience : the official journal of the Society for Neuroscience* **33**, 722-733 (2013).
14. M. C. Reddan, T. D. Wager, D. Schiller, Attenuating Neural Threat Expression with Imagination. *Neuron* **100**, 994-1005 e1004 (2018).
15. O. Klavir, R. Genud-Gabai, R. Paz, Functional connectivity between amygdala and cingulate cortex for adaptive aversive learning. *Neuron* **80**, 1290-1300 (2013).

16. O. Dal Monte, C. C. J. Chu, N. A. Fagan, S. W. C. Chang, Specialized medial prefrontal-amygdala coordination in other-regarding decision preference. *Nature neuroscience* **23**, 565-574 (2020).
17. S. A. Allsop *et al.*, Corticoamygdala Transfer of Socially Derived Information Gates Observational Learning. *Cell* **173**, 1329-1342 e1318 (2018).
18. L. J. Gabard-Durnam *et al.*, The development of human amygdala functional connectivity at rest from 4 to 23 years: a cross-sectional study. *NeuroImage* **95**, 193-207 (2014).
19. D. G. Gee *et al.*, Neurocognitive Development of Motivated Behavior: Dynamic Changes across Childhood and Adolescence. *The Journal of neuroscience : the official journal of the Society for Neuroscience* **38**, 9433-9445 (2018).
20. M. J. Kim, D. G. Gee, R. A. Loucks, F. C. Davis, P. J. Whalen, Anxiety dissociates dorsal and ventral medial prefrontal cortex functional connectivity with the amygdala at rest. *Cereb Cortex* **21**, 1667-1673 (2011).
21. C. A. Burghy *et al.*, Developmental pathways to amygdala-prefrontal function and internalizing symptoms in adolescence. *Nature neuroscience* **15**, 1736-1741 (2012).
22. H. Johansen-Berg *et al.*, Anatomical connectivity of the subgenual cingulate region targeted with deep brain stimulation for treatment-resistant depression. *Cereb Cortex* **18**, 1374-1383 (2008).
23. B. A. Vogt, L. Vogt, N. B. Farber, G. Bush, Architecture and neurocytology of monkey cingulate gyrus. *The Journal of comparative neurology* **485**, 218-239 (2005).
24. P. H. Rudebeck *et al.*, A role for primate subgenual cingulate cortex in sustaining autonomic arousal. *Proceedings of the National Academy of Sciences of the United States of America* **111**, 5391-5396 (2014).
25. P. L. Lockwood, M. K. Wittmann, Ventral anterior cingulate cortex and social decision-making. *Neuroscience and biobehavioral reviews* **92**, 187-191 (2018).
26. M. A. Apps, M. F. Rushworth, S. W. Chang, The Anterior Cingulate Gyrus and Social Cognition: Tracking the Motivation of Others. *Neuron* **90**, 692-707 (2016).
27. N. Palomero-Gallagher, K. Zilles, Cyto- and receptor architectonic mapping of the human brain. *Handb Clin Neurol* **150**, 355-387 (2018).
28. U. Livneh, J. Resnik, Y. Shohat, R. Paz, Self-monitoring of social facial expressions in the primate amygdala and cingulate cortex. *Proceedings of the National Academy of Sciences of the United States of America* **109**, 18956-18961 (2012).
29. K. Amemori, A. M. Graybiel, Localized microstimulation of primate pregenual cingulate cortex induces negative decision-making. *Nature neuroscience* **15**, 776-785 (2012).
30. M. Modirrousta, L. K. Fellows, Dorsal medial prefrontal cortex plays a necessary role in rapid error prediction in humans. *The Journal of neuroscience : the official journal of the Society for Neuroscience* **28**, 14000-14005 (2008).
31. L. J. Freedman, T. R. Insel, Y. Smith, Subcortical projections of area 25 (subgenual cortex) of the macaque monkey. *Journal of Comparative Neurology* **421**, 172-188 (2000).
32. A. J. McDonald, J. F. Muller, F. Mascagni, GABAergic innervation of alpha type II calcium/calmodulin-dependent protein kinase immunoreactive pyramidal neurons in the rat basolateral amygdala. *The Journal of comparative neurology* **446**, 199-218 (2002).
33. I. Petrof, S. M. Sherman, Functional significance of synaptic terminal size in glutamatergic sensory pathways in thalamus and cortex. *The Journal of physiology* **591**, 3125-3131 (2013).
34. N. Palomero-Gallagher *et al.*, Functional organization of human subgenual cortical areas: Relationship between architectonical segregation and connectional heterogeneity. *NeuroImage* **115**, 177-190 (2015).
35. F. X. Neubert, R. B. Mars, J. Sallet, M. F. Rushworth, Connectivity reveals relationship of brain areas for reward-guided learning and decision making in human and monkey

frontal cortex. *Proceedings of the National Academy of Sciences of the United States of America* **112**, E2695-2704 (2015).
36. M. F. S. Rushworth, R. B. Mars, J. Sallee, Are there specialized circuits for social cognition and are they unique to humans? *Curr Opin Neurobiol* **23**, 436-442 (2013).
37. T. Chiba, T. Kayahara, K. Nakano, Efferent projections of infralimbic and prelimbic areas of the medial prefrontal cortex in the Japanese monkey, Macaca fuscata. *Brain research* **888**, 83-101 (2001).
38. A. R. Damasio, The somatic marker hypothesis and the possible functions of the prefrontal cortex. *Philosophical transactions of the Royal Society of London. Series B, Biological sciences* **351**, 1413-1420 (1996).
39. Y. Chudasama *et al.*, The role of the anterior cingulate cortex in choices based on reward value and reward contingency. *Cereb Cortex* **23**, 2884-2898 (2013).
40. H. Barbas, H. Ghashghaei, S. M. Dombrowski, N. L. Rempel-Clower, Medial prefrontal cortices are unified by common connections with superior temporal cortices and distinguished by input from memory-related areas in the rhesus monkey. *Journal of Comparative Neurology* **410**, 343-367 (1999).
41. M. K. P. Joyce, H. Barbas, Cortical Connections Position Primate Area 25 as a Keystone for Interoception, Emotion, and Memory. *The Journal of neuroscience : the official journal of the Society for Neuroscience* **38**, 1677-1698 (2018).
42. P. H. Rudebeck, M. J. Buckley, M. E. Walton, M. F. Rushworth, A role for the macaque anterior cingulate gyrus in social valuation. *Science* **313**, 1310-1312 (2006).
43. R. Pryluk *et al.*, Shared yet dissociable neural codes across eye gaze, valence and expectation. *Nature* **586**, 95-100 (2020).
44. A. Etkin, T. Egner, D. M. Peraza, E. R. Kandel, J. Hirsch, Resolving emotional conflict: a role for the rostral anterior cingulate cortex in modulating activity in the amygdala. *Neuron* **51**, 871-882 (2006).
45. T. Ito *et al.*, Neural basis of negativity bias in the perception of ambiguous facial expression. *Scientific reports* **7**, 420 (2017).
46. M. E. Maier, G. di Pellegrino, Impaired conflict adaptation in an emotional task context following rostral anterior cingulate cortex lesions in humans. *Journal of cognitive neuroscience* **24**, 2070-2079 (2012).
47. E. A. Phelps, M. R. Delgado, K. I. Nearing, J. E. LeDoux, Extinction learning in humans: role of the amygdala and vmPFC. *Neuron* **43**, 897-905 (2004).
48. G. J. Quirk, J. S. Beer, Prefrontal involvement in the regulation of emotion: convergence of rat and human studies. *Curr Opin Neurobiol* **16**, 723-727 (2006).
49. R. Genud-Gabai, O. Klavir, R. Paz, Safety signals in the primate amygdala. *The Journal of neuroscience : the official journal of the Society for Neuroscience* **33**, 17986-17994 (2013).
50. C. Buchel, J. Morris, R. J. Dolan, K. J. Friston, Brain systems mediating aversive conditioning: an event-related fMRI study. *Neuron* **20**, 947-957 (1998).
51. J. S. Morris *et al.*, A differential neural response in the human amygdala to fearful and happy facial expressions. *Nature* **383(6603)**, 812-815 (1996).
52. H. C. Breiter *et al.*, Response and habituation of the human amygdala during visual processing of facial expression. *Neuron* **17**, 875-887 (1996).
53. D. A. Fitzgerald, M. Angstadt, L. M. Jelsone, P. J. Nathan, K. L. Phan, Beyond threat: amygdala reactivity across multiple expressions of facial affect. *NeuroImage* **30**, 1441-1448 (2006).
54. S. W. Chang *et al.*, Neural mechanisms of social decision-making in the primate amygdala. *Proceedings of the National Academy of Sciences of the United States of America* **112**, 16012-16017 (2015).

55. K. M. Gothard *et al.*, New perspectives on the neurophysiology of primate amygdala emerging from the study of naturalistic social behaviors. *Wiley Interdiscip Rev Cogn Sci* **9** (2018).
56. J. Minxha *et al.*, Fixations Gate Species-Specific Responses to Free Viewing of Faces in the Human and Macaque Amygdala. *Cell reports* **18**, 878-891 (2017).
57. P. T. Putnam, K. M. Gothard, Multidimensional Neural Selectivity in the Primate Amygdala. *eNeuro* **6** (2019).
58. N. H. Kalin, S. E. Shelton, Defensive behaviors in infant rhesus monkeys: environmental cues and neurochemical regulation. *Science* **243**, 1718-1721 (1989).
59. M. Brinley-Reed, F. Mascagni, A. J. McDonald, Synaptology of prefrontal cortical projections to the basolateral amygdala: an electron microscopic study in the rat. *Neuroscience letters* **202**, 45-48 (1995).
60. K. L. Villa, E. Nedivi, "Excitatory and Inhibitory Synaptic Placement and Functional Implications". (Soringer, Japan, 2016), 10.1007/978-4-431-56050-0_18 chap. 18, pp. 467-487.
61. W. M. DeBello *et al.*, Input clustering and the microscale structure of local circuits. *Front Neural Circuits* **8**, 112 (2014).
62. M. Arruda-Carvalho, W. C. Wu, K. A. Cummings, R. L. Clem, Optogenetic Examination of Prefrontal-Amygdala Synaptic Development. *The Journal of neuroscience : the official journal of the Society for Neuroscience* **37**, 2976-2985 (2017).
63. H. Bouwmeester, G. Wolterink, J. M. van Ree, Neonatal development of projections from the basolateral amygdala to prefrontal, striatal, and thalamic structures in the rat. *The Journal of comparative neurology* **442**, 239-249 (2002).
64. A. Holtmaat, L. Wilbrecht, G. W. Knott, E. Welker, K. Svoboda, Experience-dependent and cell-type-specific spine growth in the neocortex. *Nature* **441**, 979-983 (2006).
65. M. Sheng, E. Kim, The postsynaptic organization of synapses. *Cold Spring Harbor perspectives in biology* **3** (2011).
66. G. M. Innocenti, R. Caminiti, Axon diameter relates to synaptic bouton size: structural properties define computationally different types of cortical connections in primates. *Brain structure & function* **222**, 1169-1177 (2017).
67. V. N. Murthy, T. J. Sejnowski, C. F. Stevens, Heterogeneous release properties of visualized individual hippocampal synapses. *Neuron* **18**, 599-612 (1997).
68. C. Rosenmund, C. F. Stevens, Definition of the readily releasable pool of vesicles at hippocampal synapses. *Neuron* **16**, 1197-1207 (1996).
69. Y. Yang, J. Lu, Y. Zuo, Changes of synaptic structures associated with learning, memory and diseases. *Brain Science Advances* **4(2)**, 99-117 (2018).
70. K. K. Cover, B. N. Mathur, Axo-axonic synapses: Diversity in neural circuit function. *The Journal of comparative neurology* 10.1002/cne.25087 (2020).
71. F. Grabenhorst, R. Baez-Mendoza, W. Genest, G. Deco, W. Schultz, Primate Amygdala Neurons Simulate Decision Processes of Social Partners. *Cell* **177**, 986-998 e915 (2019).
72. K. M. Gothard, Multidimensional processing in the amygdala. *Nature reviews. Neuroscience* **21**, 565-575 (2020).
73. D. G. Amaral, J. L. Bassett, Cholinergic innervation of the monkey amygdala: An immunohistochemical analysis with antisera to choline acetyltransferase. *J. Comp. Neurol.* **281**, 337-361 (1989).
74. F. G. Wouterlood, A. J. Boekel, G. A. Meijer, J. A. Belien, Computer-assisted estimation in the CNS of 3D multimarker 'overlap' or 'touch' at the level of individual nerve endings: a confocal laser scanning microscope application. *Journal of neuroscience research* **85**, 1215-1228 (2007).

75. M. Ashaber *et al.*, Synaptic organization of cortico-cortical communication in primates. *The European journal of neuroscience* **52**, 4037-4056 (2020).

Figures

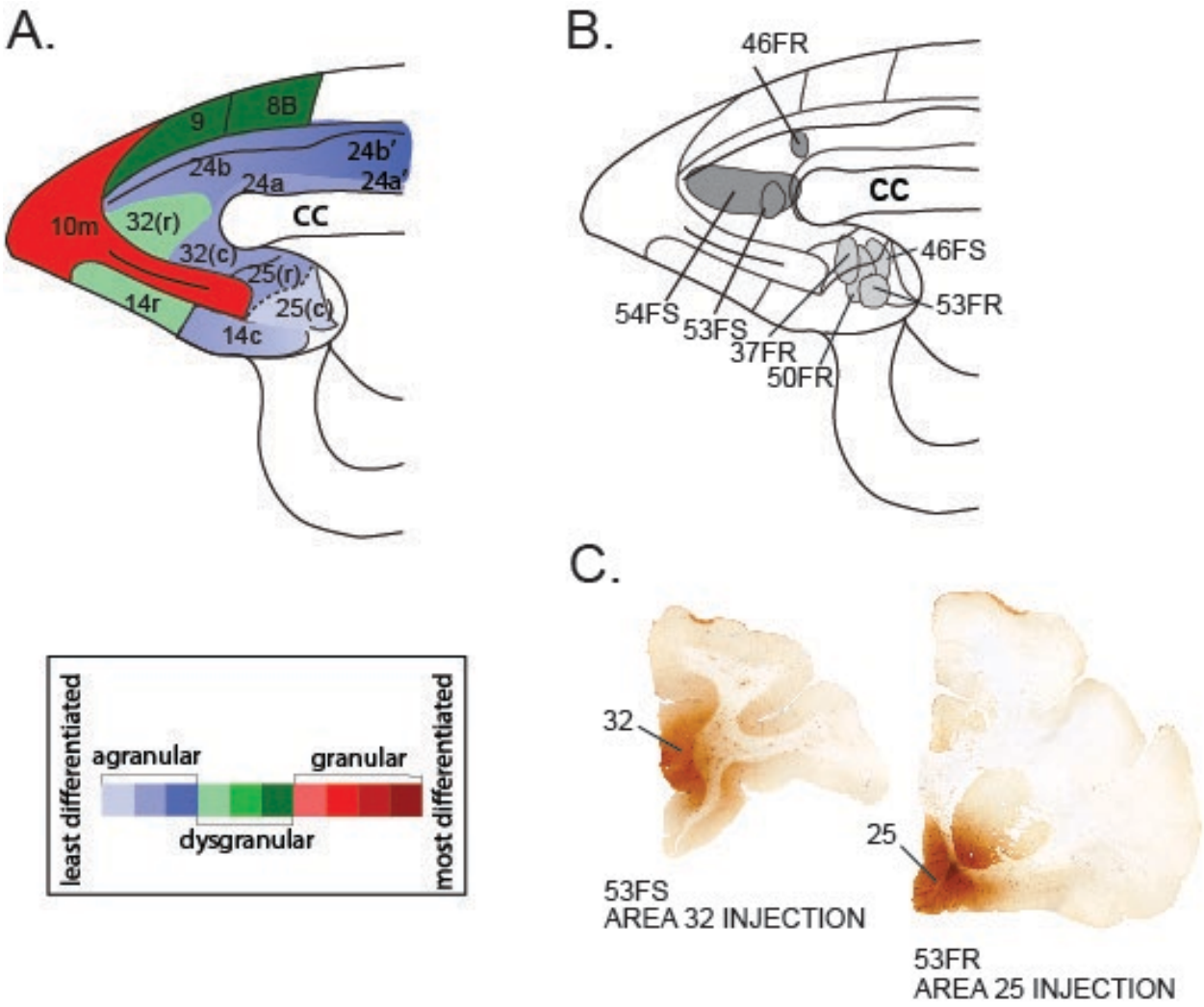

Figure 1.

Brodmann area locations of the sgACC (area 25/14c) and pgACC (area 24b, 32) in sagittal section of the prefrontal cortex. Note granularity shifts across the region. Agranular (blue), dysgranular (green) and granular (red). (B) Sagittal schematic of showing placement of anterograde injection sites. (C) Brightfield images of dual tracer injections into area 32 and area 25 in the same hemisphere of Case 53. (Following the area 25 injection, anterogradely labeled fibers are seen leaving the cortex, and entering the ventral striatum).

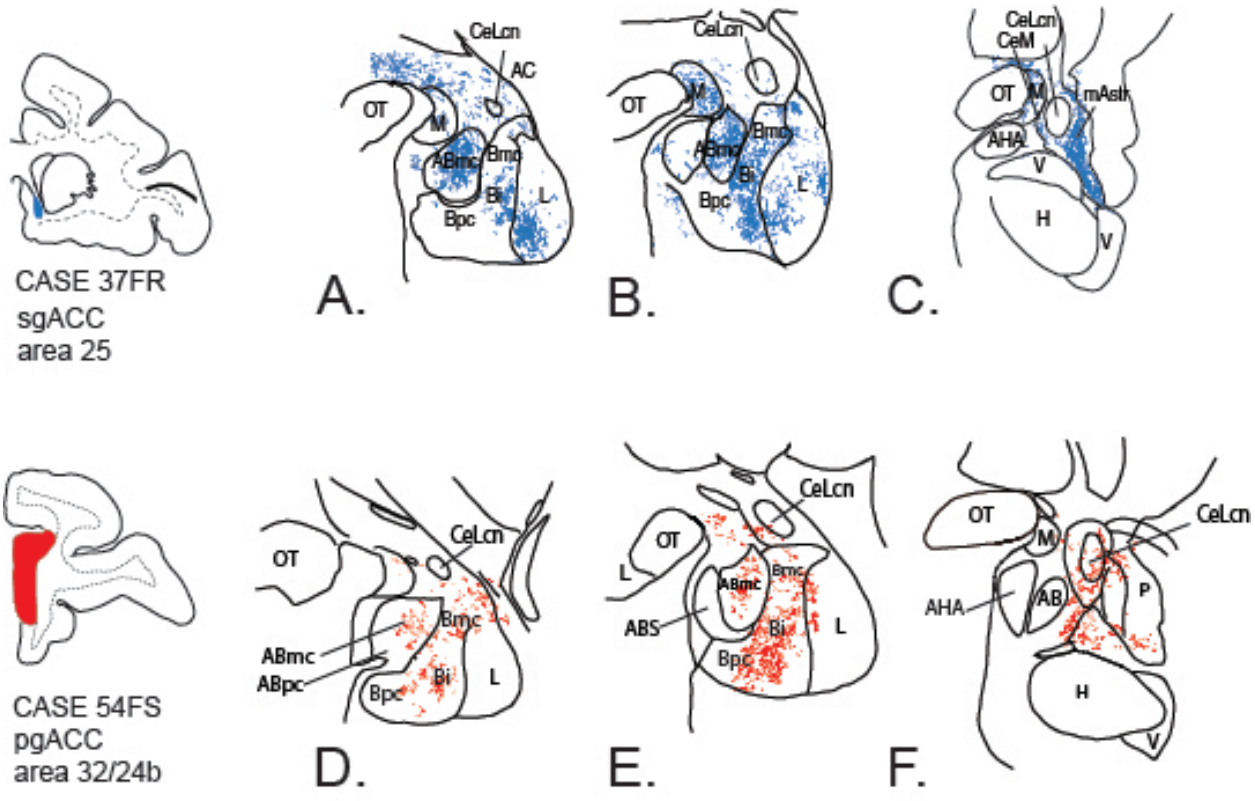

Figure 2.

Distribution of anterogradely labeled fibers in two different cases after injections into sgACC (A-C) (area 25, blue) and pgACC (red) (D-F). The injection in the pgACC was three times larger than other injections, encompassing areas 32/24b. ***Abbrs.*** **ABmc**, accessory basal nucleus, magnocellular subdivision; **ABpc**, accessory basal nucleus, parvicellular subdivision; **ABs**, accessory basal nucleus, sulcal subdivision; **AC**, anterior commissure; **AHA**, amygdalohippocampal region; **Bi**, basal nucleus, intermediate subdivision; **Bmc**, basal nucleus, magnocellular subdivision; **Bpc**, basal nucleus, parvicellular subdivision; **CeLcn**, lateral subdivision of the central nucleus; **H**, hippocampus; **L**, lateral nucleus; **M**, medial nucleus; **mAstr**, medial amygdalostriatal area; **OT**, optic tract; **P**, putamen; **V**, ventricle;

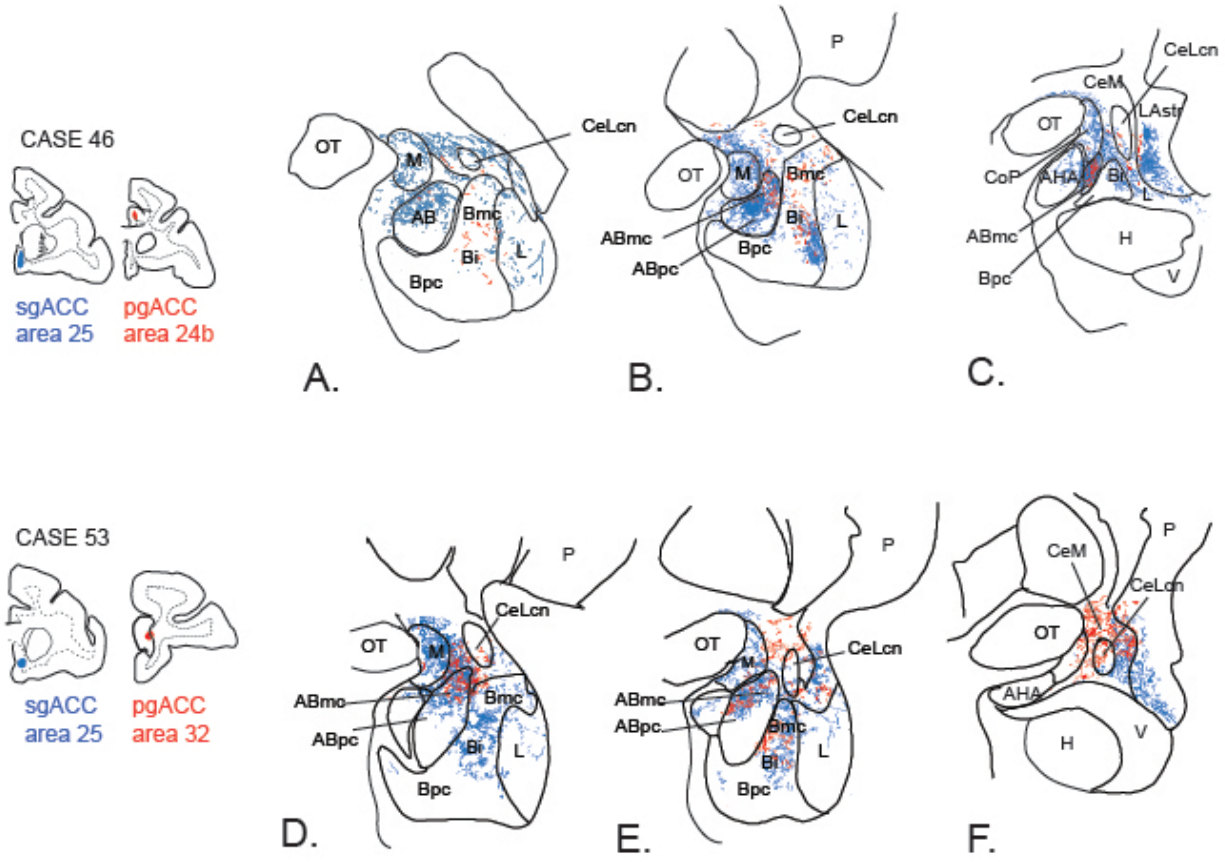

Figure 3.

Anterogradely labeled fiber distribution following *paired* pg- and sgACC tracer injections. Rostral to caudal distribution of sgACC (blue) and pgACC (red) fibers in Case 46 (A-C) and 53 (D-F). sgACC fibers were densely distributed throughout several amygdalar nuclei; pgACC displayed a sparser distribution with densest fiber concentrations, overlapping terminals from the sgACC in the ABmc and Bi. Abbreviations, see Fig. 2.

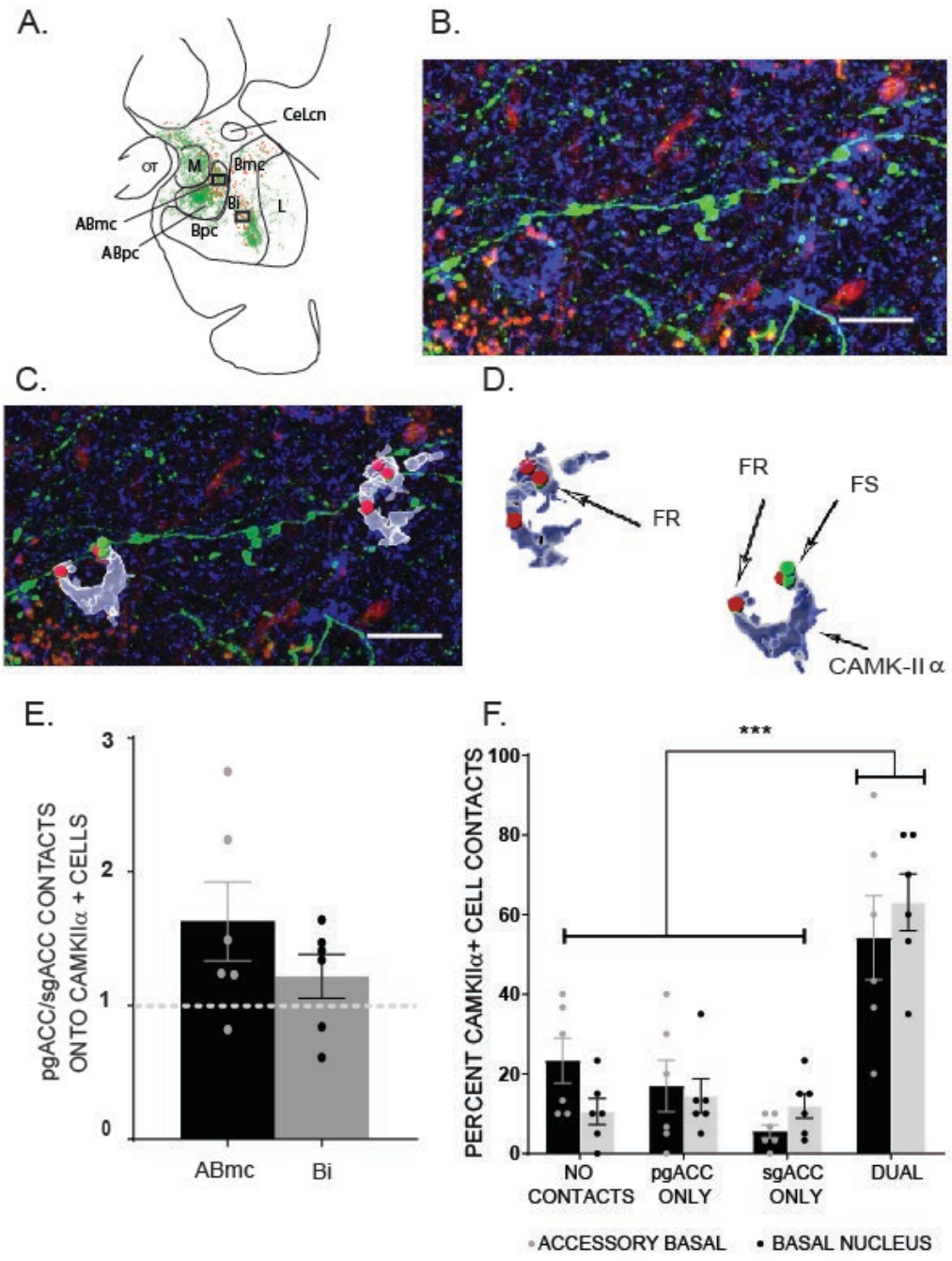

Figure 4.

Triple immunofluorescent analysis and quantification of tracer contacts following paired pgACC/sgACC injections. (A) Camera lucida rendering of anterograde fiber distribution following pgACC (red) and sgACC (green) injections, used for selection and registration of 'hotspots' in the ABmc and Bi (boxed areas). (B) CAMK-IIα (blue), fluoroscein tracer (FS) and fluoruby tracer (FR) triple immunofluorescent confocal micrograph collected in the ABmc 'hotpspot', boxed area in A. Scale bar = 10 um (C) Overlay of Imaris software 'surface' (CAMK-IIα) and 'spot' (tracer)

renderings onto confocal micrograph (shown in B). Scale bar = 10 um (D) Imaris rendered objects depicting sites of tracer contact with CAMK-IIα cells. (E) The proportion of pgACC/sgACC contacts onto all CAMK-IIα cells counted in the ABmc and Bi 'hotspots'. (F) The proportion of CAMK-IIα cells with no contact, single contacts, or dual contacts from pgACC and sgACC anterogradely labeled fibers in the ABmc and Bi (****= $p<0.001$, two way ANOVA with Tukey multiple comparisons post hoc test)

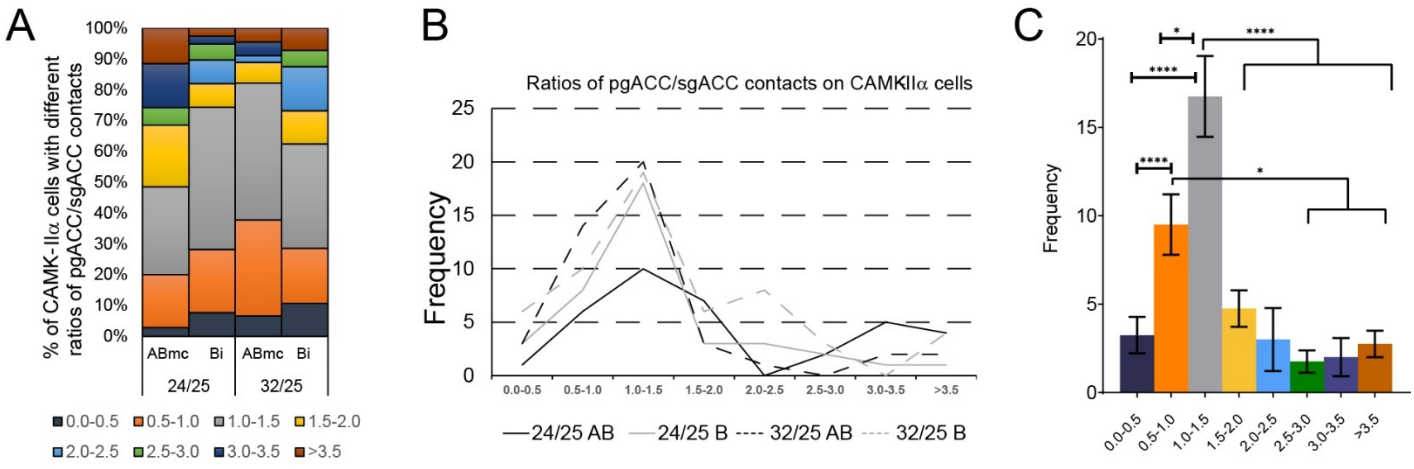

Figure 5.

The proportion of pgACC to sgACC dual contacts are tightly balanced in amygdalar hotspots. (A) Binned ratios of pgACC/sgACC contacts onto individual dual-contacted CAMK-IIα cells. A large percentage of CAMK-IIα cells had ratios 1:1 pgACC-to-sgACC contacts (gray bars) in both the ABmc and Bi. (B) Frequency distribution of pgACC/sgACC contacts onto CAMK-IIα cells. Ratio bins range from 0 to >3.5. (C) Quantitative comparisons of ratio bin counts (*=p<0.05,****= p<0.001, one way ANOVA with Tukey multiple comparisons post hoc test).

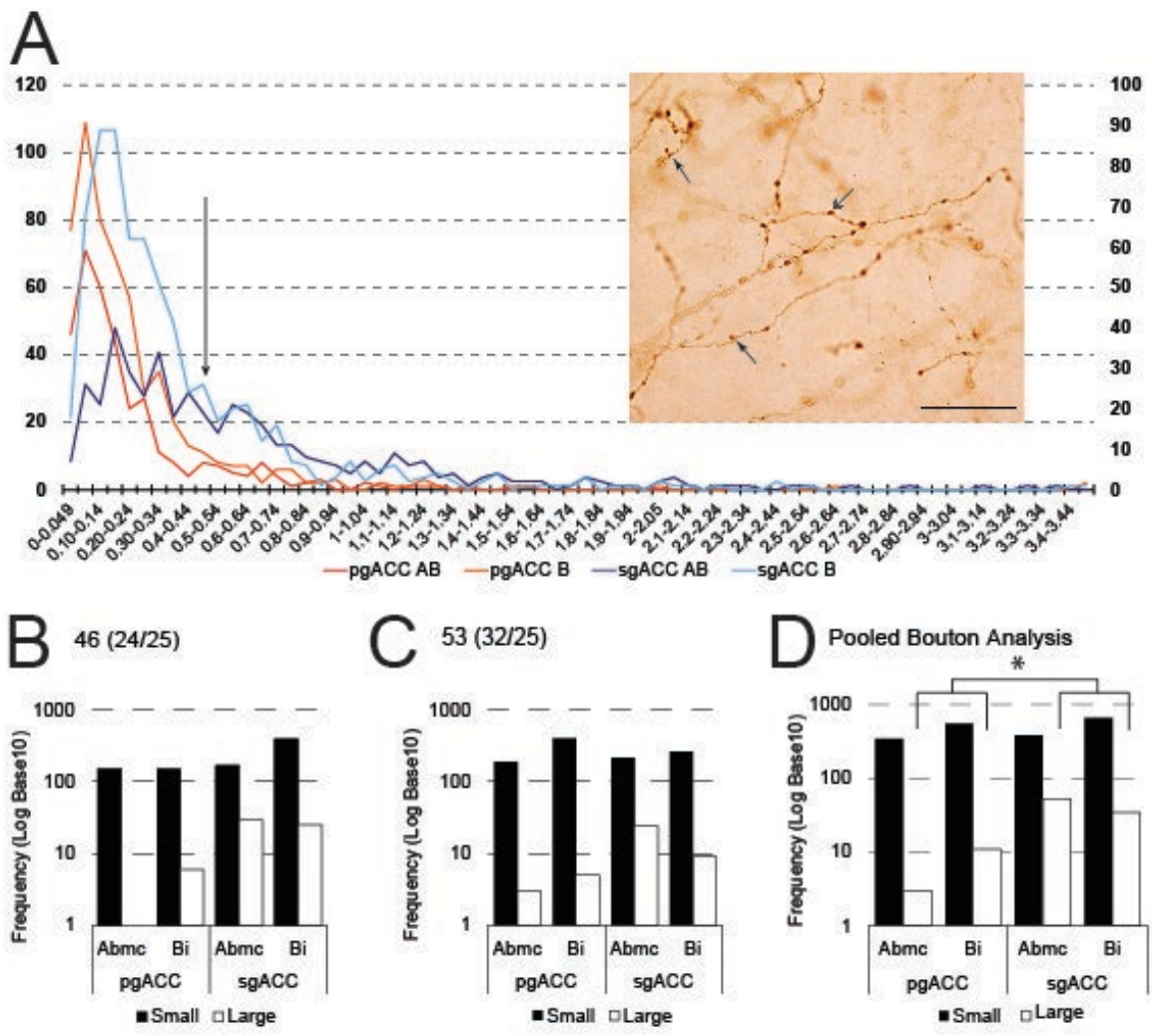

Figure 6.

Unbiased stereology and quantitative analysis of anterogradely labeled synaptic boutons at 100x. (A) Frequency bin representation of volumetric measurements of tracer-labeled synaptic boutons from the sgACC (blue) and pgACC (red) in 'hotspots'. Volume bins ranged from 0->3.45 um^3. Many boutons fell below 0.52 um^3 for all projections (arrow denotes shift to large categorized boutons). (A, inset) A representative brightfield micrograph of anterograde tracer-labeled fibers in the basal nucleus showing bouton types. Terminal boutons (single arrowhead) were characterized by a distinct swelling with an apparent stalk emanating from the axon terminal. *En passant boutons* (double arrowhead) displayed a characteristic swelling along the terminal fiber. Scale bar= 25 um. (B- C) Log frequency of small (black bars) vs large bouton (white bars) comparisons for each case with paired injections: (B) Case 46 (areas 24/25) (C) Case 53 (areas 32/25) (D) Pooled analyses, both cases. Large boutons (greater than 0.52 um^3

volume) were significantly more frequent on axons originating from sgACC. Unpaired student t-test, *= p=0.0103.